nature geoscience

Article

https://doi.org/10.1038/s41561-023-01186-3

Slow slip along the Hikurangi margin linked to fluid-rich sediments trailing subducting seamounts

Received: 8 September 2022

Accepted: 20 April 2023

Published online: 05 June 2023



Nathan L. Bangs ®¹ ⋈, Julia K. Morgan ®², Rebecca E. Bell³, Shuoshuo Han ®¹, Ryuta Arai ®⁴, Shuichi Kodaira ®⁴, Andrew C. Gase ®¹, Xinming Wu ®⁵, Richard Davy ®³, Laura Frahm ®³, Hannah L. Tilley ^{6,7}, Daniel H. N. Barker⁸, Joel H. Edwards ^{9,10}, Harold J. Tobin ®¹¹, Tim J. Reston ®¹², Stuart A. Henrys ®³, Gregory F. Moore ®⁶, Dan Bassett ®³, Richard Kellett ®³, Valerie Stucker ®³ & Bill Fry ®³

Large seamounts and basement relief cause permanent deformation when they collide with the overriding plate at subduction zones. The resulting structural and compositional heterogeneities have been implicated as controlling factors in megathrust slip behaviour. Subducting seamounts may temporarily lock plates, favouring subsequent large earthquakes. Alternatively, seamounts may redistribute stress, reducing seismic slip. Here we present three-dimensional seismic data from the seamount-studded subducting Hikurangi Plateau along New Zealand's North Island. We find that one well-imaged seamount, the Papaku Seamount, locally uplifts the overriding plate and leaves a tube-shaped lens of sediment trailing in its wake. Anomalously low seismic velocities within and below the Pāpaku lens and along the megathrust fault are consistent with the presence of unconsolidated, overpressured fluid-rich sediments. Similar observations from an older sediment lens, which corresponds to the location of a 2014 slow-slip rupture event, suggest that such overpressures can persist along the megathrust due to delayed drainage out of the subducting plate. The collocation of the 2014 slow-slip earthquake with this sediment lens suggests that these fluid-rich regions define zones that enable slow slip. We hypothesize that sediment lenses left behind by subducting seamounts can create low-effective-stress patches within transitionally stable marine sediment along the megathrust that are conducive to slow slip.

Seamount collisions along forearcs are known to leave behind distinctive signatures in margin structure and rock properties. On the seafloor, large circular embayments, landslide scars and uplifted seafloor ridges are linked to rough topography on the subducting crust (for example, Costa Rica¹). Where seamounts underthrust the forearc, they have been interpreted to generate distinctive

three-dimensional (3D) patterns of normal faults^{2,3}, enhance slip on existing thrusts⁴, initiate out-of-sequence thrust faults^{5,6} or cause shifts in the décollement⁷. All of these interactions can disrupt accretionary wedge thrust sequences⁸, impact physical properties⁵ or complicate fluid migration patterns that govern stress and deformation within the margin⁹.

A full list of affiliations appears at the end of the paper. —e-mail: nathan@ig.utexas.edu

More mysteriously, however, relief on the subducting crust appears to control megathrust mechanical behaviour in ways that models and observations have yet to resolve. Settings where rough subducting crust is not completely covered by sediments, such as northern Hikurangi, Costa Rica, Ryuku and along the Japan trench, exhibit a wide range of slip behaviours, including slow-slip events (SSEs), thus implicating seamounts in controlling slip^{10–13}. Various explanations have been proposed for how seamounts create a structurally complex, heterogeneous interface that regulates slip in patches along the megathrust. In one role, seamounts are structural asperities that temporarily lock the plate boundary and then slip during earthquakes¹⁴. More recently, seamounts have been interpreted to contribute to aseismic slip by inducing complex fracture networks within the overriding plate¹⁵. However, these current models do not explain the low effective stress in a setting with transitional frictional stability that is required for slow slip¹⁶. Seamounts appear to have a role in the occurrence of SSEs for reasons beyond our current understanding.

Shallow SSEs and seamounts coincide in many subduction zones globally. For example, they have been reported along a segment of the Ecuadorian margin¹⁷, known for seamount and basement ridge collision¹⁸, and the Nankai Trough¹⁹. These links are intriguing; however, due to limited offshore geodetic constraints on slip that can be linked directly to structural and hydrogeologic effects of seamount collision, we have yet to determine how seamounts generate conditions conducive for SSEs. Recent investigations along New Zealand's Hikurangi subducting margin are beginning to make these links.

The source regions of SSEs along the east coast of New Zealand's North Island are shallow (<15 km) relative to deep (>25 km) SSEs found in other settings (for example, ref. 20) and provide the best documented, regularly repeating SSEs globally21. Furthermore, geophysical investigations along the margin are providing clues to the sources of macroscale heterogeneity contributing to SSEs along the plate interface. Here the subducting Cretaceous Hikurangi Plateau large igneous province is dotted with seamounts that protrude above ~1 km of Palaeocene-Pliocene pelagic carbonate drape and overlying Pliocene-Recent clastic trench sediments^{22,23}. At depth, an actively subducting seamount with a strong magnetic anomaly across the mid-slope basin²⁴ is proposed to have subducted >5 km below seafloor^{25,26}. The collocation of SSE ruptures with zones of high seismic reflectivity down dip of seamounts led researchers to hypothesize that the unusually shallow slow slip that occurs along the Hikurangi margin stems from high fluid pressures developed within patches of fluid-rich sediment^{25,27} that may have transitional frictional stability¹⁶ down dip of subducting seamounts.

To date, however, researchers have not been able to resolve the full impacts of seamount subduction on forearc damage, deformation and rock physical properties needed to assess potential links between seamounts and SSEs implied by their collocation. Typical 2D seismic profiles cannot capture the 3D complexity of forearc structures and rarely provide adequate constraints about the associated rock properties; 3D seismic data are necessary for capturing seamount collision processes (for example, Nankai²8). To clarify links among subducting seamounts, deformation and slip, we acquired a 3D seismic-data volume using four 6-km-long receiver arrays, a 3,300 inch³ (54 l) seismic source array on the RV *Langseth* and 97 JAMSTEC ocean-bottom seismometers (OBSs) across a $15 \times 60 \text{ km}^2$ area of the Hikurangi margin offshore Gisborne, New Zealand (Fig. 1 and Extended Data Fig. 7). The resolution and coverage from the 3D volume are well suited to examine seamount collision.

The 3D signature of seamount collision

Two profiles across the lower slope, $11\,\mathrm{km}$ apart, taken from northern and southern ends of the 3D seismic volume show contrasting effects of seamounts on forearc deformation. Along seismic Line 774 in the north (Fig. 2a and Extended Data Fig. 1), we see two very long thrust

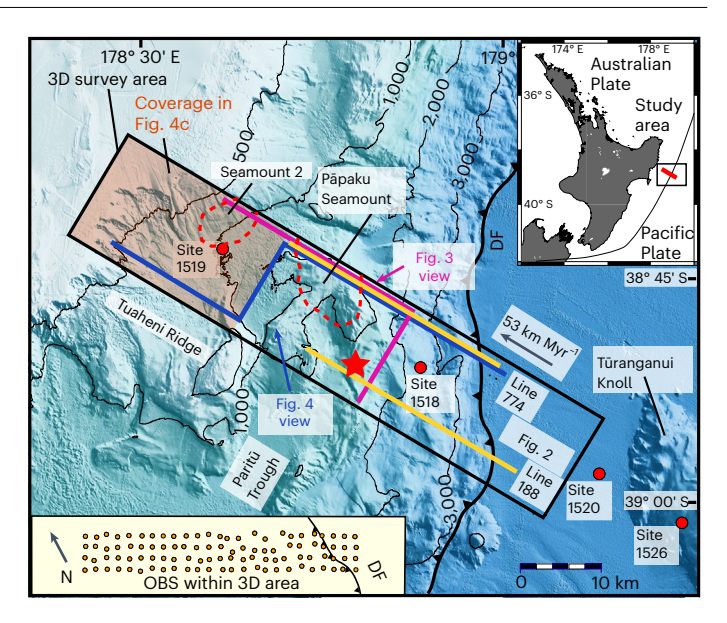


Fig. 1| Bathymetric map of the Hikurangi margin. Location on regional map shown in upper inset. Depth contours (thin black lines) in metres. The NZ3D survey area (black rectangle) is $15 \times 60 \text{ km}^2$ and extends from the trench to the shelf. Red dashed lines are seamount locations for the Pāpaku and a second seamount (Seamount 2). Coloured lines show seismic profiles shown in figures with colours corresponding to labels of figure viewpoints (coloured arrows). Shaded area shows coverage of the décollement in Fig. 4c. Orange circles in lower inset are OBS locations within the 3D survey. Red circles are Expedition 372/375 drill sites. Red star marks the epicentre of the 1947 moment magnitude 7.0 offshore Poverty Bay tsunami earthquake 24 . Black arrow shows relative convergence direction. DF, deformation front.

sheets (up to 20 km), one apparently stacked on the other. The deeper one is bounded at its base by the low-angle décollement fault, which emerges onto the seafloor along the most frontal thrust. The shallower thrust sheet is separated from the deeper one by a long (~15 km) low-angle (<10°) thrust fault, the Pāpaku fault, which was drilled during the International Ocean Discovery Program Expeditions 372/375~5 km to the south²⁹. The apparent duplication of trench sediments across the Pāpaku fault on this profile indicates fault displacement of at least 15 km. By contrast, seismic Line 188 exhibits a very different structure (Fig. 2b and Extended Data Fig. 2). Several high-angle thrusts (~30°) have imbricated the frontal strata to construct a more typical accretionary wedge. Offsets along the faults increase progressively landwards, from a few 100 m at the deformation front to several kilometres on the more landward thrusts. In contrast to the north, each thrust exhibits clear footwall cut-offs along the ramps and incipient or well-developed fault-bend folds in the hanging-wall sequences.

Important clues to the origins of these contrasting structures are found in the geometry of the underlying décollement. The thrust faults on the southern profile sole into an interval of subhorizontal reflectors that separate the accretionary wedge from the subducting Hikurangi Plateau. The décollement is thought to form within the pelagic sequences, or immediately below them within the underlying volcaniclastic sequences²², which we presume cause the reflectivity near the décollement and beneath it. To the north, the three thrust faults that bound the two lengthy thrust sheets converge near an ~10 km wide structural high that we interpret to be a subducted seamount. This feature is ~2 km high with steep dips of ~25° and ~20° on its landward and seaward flanks, respectively, and peaks at 4,650 m below the sea surface. This may be the $peak \, of a \, broader \, construction^{25,27,30} \, (Supplementary \, Fig. 1 \, and \, Extended \, and \, Construction \, (Supplementary \, Fig. 1 \, and \, Extended \, Construction \, (Supplementary \, Fig. 1 \, and \, Extended \, Construction \, (Supplementary \, Fig. 1 \, and \, Extended \, Construction \, (Supplementary \, Fig. 1 \, and \, Extended \, Construction \, (Supplementary \, Fig. 1 \, and \, Extended \, Construction \, (Supplementary \, Fig. 1 \, and \, Extended \, Construction \, (Supplementary \, Fig. 1 \, and \, Extended \, Construction \, (Supplementary \, Fig. 1 \, and \, Extended \, Construction \, (Supplementary \, Fig. 1 \, and \, Extended \, Construction \, (Supplementary \, Fig. 1 \, and \, Extended \, Construction \, (Supplementary \, Fig. 1 \, and \, Extended \, Construction \, (Supplementary \, Fig. 1 \, and \, Extended \, Construction \, (Supplementary \, Fig. 1 \, and \, Extended \, Construction \, (Supplementary \, Fig. 1 \, and \, Extended \, Construction \, (Supplementary \, Fig. 1 \, and \, Extended \, Construction \, (Supplementary \, Fig. 1 \, and \, Construction \, (Supplementary \, Fig. 1 \,$ Data Fig. 3), which on an older profile shows its crest 2 km deeper ~8 km directly south of the summit revealed here. We name this feature Pāpaku Seamount due to its proximity to the large offset Pāpaku fault.

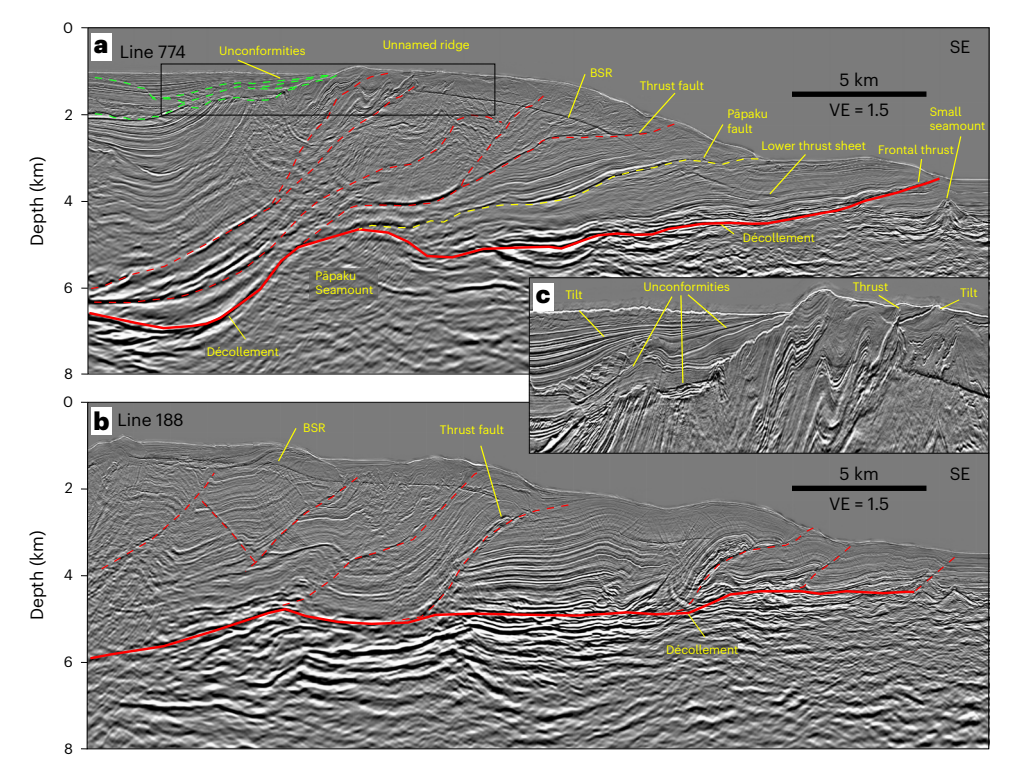


Fig. 2 | **Seismic profiles across the Hikurangi margin. a,b**, NZ3D Inline 774 along the northern end of the 3D volume (**a**) and Inline 188 across the southern end (**b**) showing the contrast in structural style with and without a subducting seamount. **c**, Enlargement of rectangle in **a**. Green dashed lines are unconformities in the

slope cover sequence. Red dashed lines are thrusts within the accretionary wedge. Solid red line traces the décollement. VE, vertical exaggeration; BSR, bottom-simulating reflection.

A crossline slice through the Pāpaku fault and bounding thrust sheets provides a clearer view of the 3D geometry of these unusual structures in an orientation close to true geometry (Fig. 3, Supplementary Fig. 3 and Extended Data Fig. 4). Of particular interest, to the south of Line 774, the Pāpaku fault slopes down to the décollement roughly mid-way across the 3D volume. The overlying strata parallel the dipping fault in both dip and strike directions, whereas the underlying trench strata remain subhorizontal and are truncated by the Pāpaku fault. The Pāpaku fault appears to curve around the flank of Pāpaku Seamount, defining a lateral ramp along its southern flank. The trench strata encompassed beneath the curved Pāpaku fault have the form of a tube-shaped sediment lens, here referred to as the Pāpaku sediment lens, which stretches seaward beneath the length of the overlying fault (Fig. 3, Extended Data Fig. 4 and Supplementary Fig. 3).

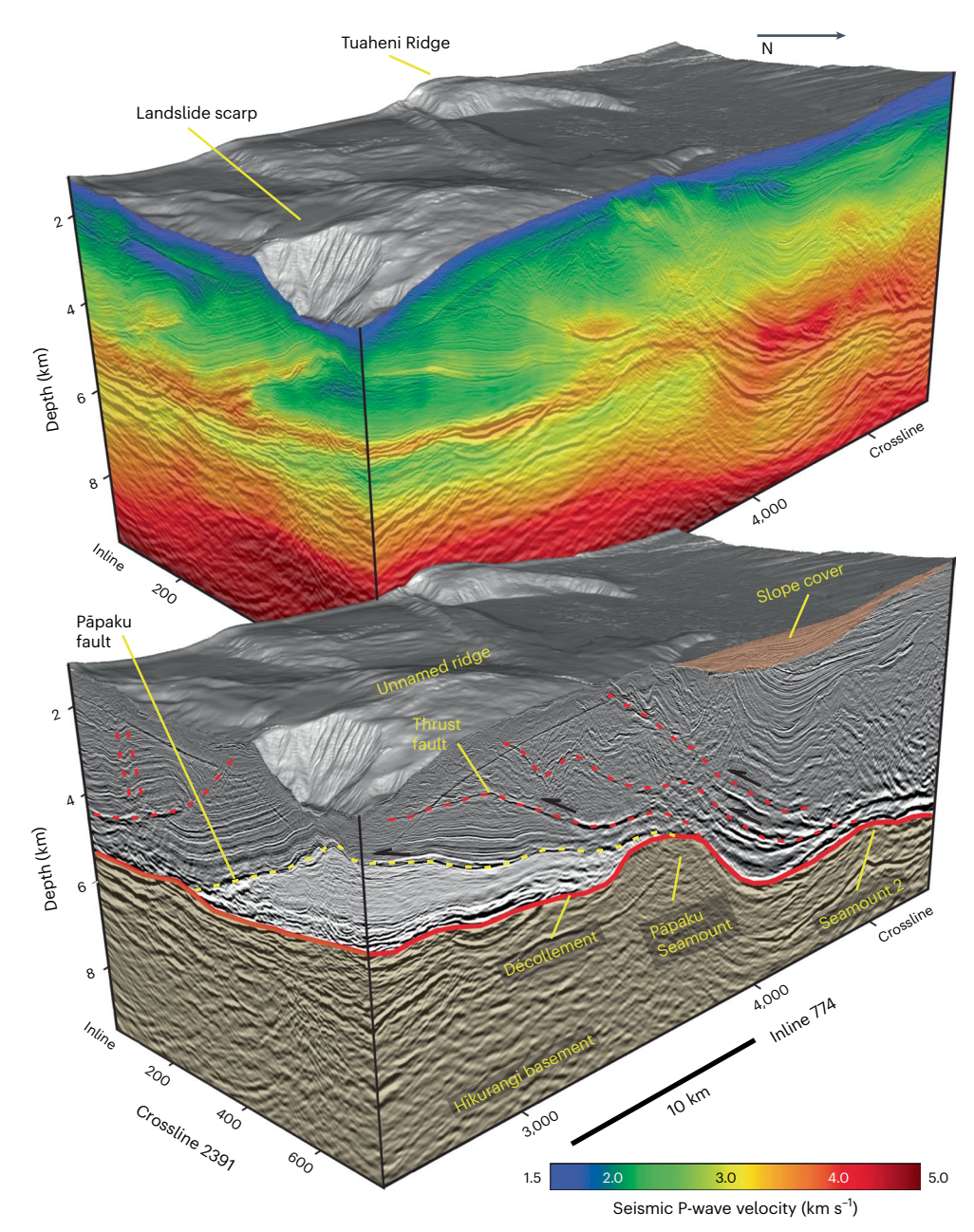
The origin of this sediment lens can be linked directly to the subducting Pāpaku Seamount. The Pāpaku fault takes off from the top of the seamount then extends seawards along a stratigraphic horizon that corresponds to the seamount height (Extended Data Fig. 4 and Supplementary Fig. 3). This places the sediment lens directly up dip and in the wake of this seamount. Clearly, the leading edge of the seamount initiated and guided the Pāpaku thrust, giving the sediment lens a cross-sectional morphology that conforms to the seamount profile.

There are several other features that hint at seamount subduction in this area. A broad unnamed seafloor ridge forms the northern terminus of the Paritū Trough directly above the interpreted seamount (Figs. 2 and 3) and may have been uplifted during its passage. As shown in Fig. 2c, unconformities and increasing stratal dips with depth within the shallow slope cover adjacent to the unnamed ridge are consistent with progressive uplift with the approaching Pāpaku Seamount. In addition, a large landslide scarp cuts the seafloor directly up dip of the seamount (Fig. 3). This landslide detached from the seaward slope of the uplifting ridge, probably in response to the passage of the

subducting seamount, and is similar to the characteristic embayments that record seamount collisions along Costa Rica¹. Despite the evidence for a passing seamount, we see little evidence of normal faults (for example, Fig. 2) predicted in sandbox and numerical models due to upper plate collapse following seamount passage (for example, ref. 2). The lack of normal faults is attributed to the presence of the Pāpaku sediment lens, which mechanically supports the upper thrust sheet in the wake of the seamount, preventing such extension.

The seismic velocity patterns in the vicinity of the Papaku sediment lens are also quite distinctive. Velocities above the Pāpaku fault and at equivalent depths south of the Pāpaku fault achieve 3.0 km s⁻¹ or more. However, within the footwall sediment, velocities are as low as 2.0 km s⁻¹ (Fig. 3). Logging-while-drilling data at Site 1518B, which penetrated the Pāpaku fault and underlying sediment lens along its southern flank, also showed an inversion in compressional (V_p) and shear wave (V_s) velocities across the fault, corresponding to an increase in porosity from ~40% in the hanging wall to as high as 70% within the shallowest 100 m below the footwall³¹. These high porosities suggest incomplete consolidation of sediments within the sediment lens and correspondingly high pore-fluid pressures, further supported by pore water solute profiles that indicate little to no fluid flow 32,33 and lab experimental tests 34. The underconsolidated and overpressured state of the footwall may result from rapid overthrusting along the Pāpaku fault as well as intense ductile sediment deformation and insufficient brittle deformation to create fracture permeability across the fault 35,36. The sediment lens also lies within the stress shadow of Pāpaku Seamount and thus is shielded from tectonic loading that would enhance consolidation9.

An important observation for conditions along the décollement is that anomalously low seismic velocities and high porosities are not limited to the sediment lens but also occur beneath the décollement. Figure 3 (see also Supplementary Figs. 4 and 5 and Extended Data Figs. 1, 2, 5 and 6) shows a low-velocity zone (<3 km s⁻¹) directly beneath the



 $\label{line:proposed} \textbf{Fig. 3} | \textbf{Perspective view of seismic volume looking southwest.} \ Shows Inline \\ 774 and Crossline 2391 (located in Fig. 1). Upper cube shows seismic P-wave velocities derived from full-waveform inversion of streamer and OBS data in 3D. Lower panel shows the same view with interpretation. Décollement (solid red line) is directed over the top of the Pāpaku Seamount. The Pāpaku fault trails in$

the wake of the Pāpaku Seamount and soles into the décollement at the seamount peak. The Pāpaku thrust is the seaward-most of a series of shallow dipping thrusts through the accretionary wedge (red dashed lines). Seamount 2 lies -10 km down dip from Pāpaku Seamount.

décollement and within the underlying volcaniclastic layer at a depth between 5 and 6 km that corresponds to the inline and crossline extent of the sediment lens. These low velocities imply similar delayed consolidation beneath the décollement as above it, defining a fluid-rich volume that surrounds the fault, with direct implications for décollement slip behaviour locally.

A history of seamount collision along the Hikurangi margin

The well-imaged example of the Pāpaku sediment lens exhibits certain features that may define signature characteristics indicative of seamount interactions. A key element is a long-offset, low-angle fault that overlies an elongate lens of unfaulted, underthrust strata bounded

by lateral thrust ramps along its flanks. Low sediment velocities occur within the lens, indicative of high pore-fluid pressures. Uplifted seafloor ridges and surficial landslides may also occur^{1,22}.

Further investigation of the 3D volume points to the occurrence of similar sets of features down dip, which suggests a long history of seamount collisions along this margin. For example, an extensive fault surface ramps through the thrust sheet that defines the hanging wall of the Pāpaku fault, carrying a highly deformed sequence of older strata (Fig. 3). We hypothesize that this thrust fault initiated along the leading edge of an earlier subducted seamount that is evident just down dip of Pāpaku seamount on Line 774 (Seamount 2).

A particularly large set of structures that also define a sediment lens stands out along the deeper portions of the accretionary wedge

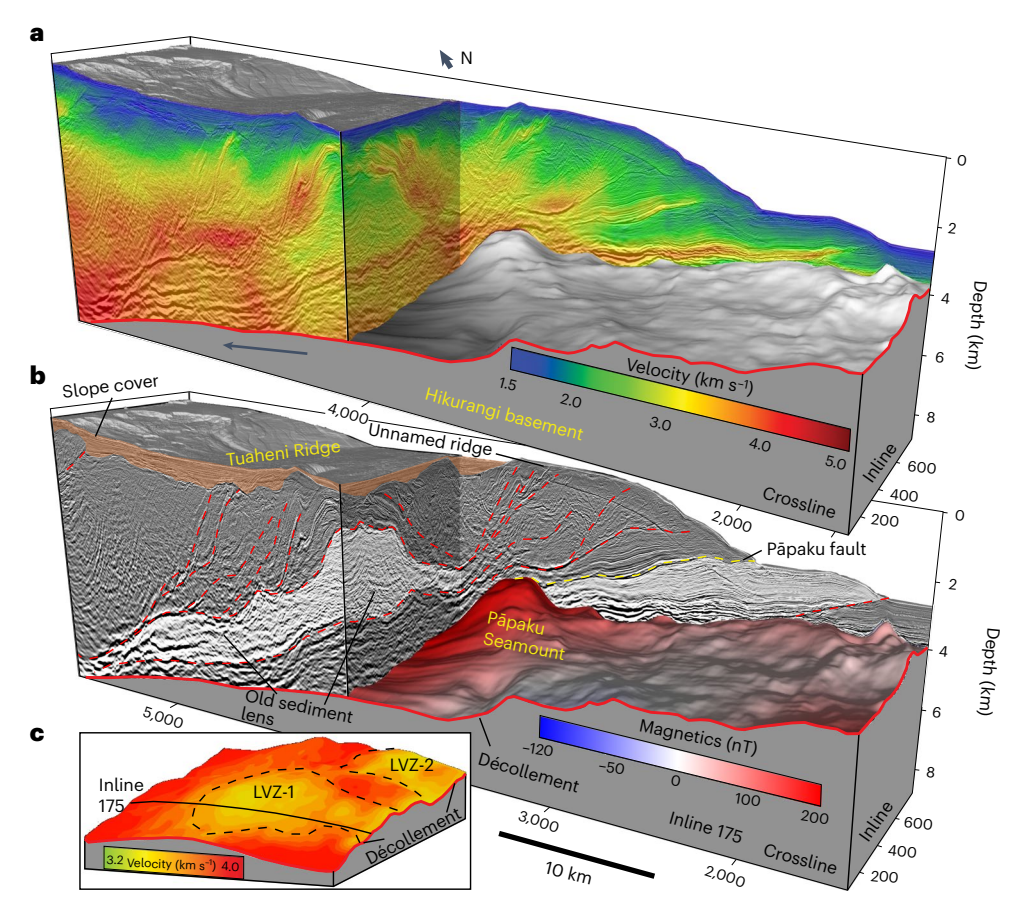


Fig. 4 | **Perspective views of the 3D volume looking northeast.** Cutaway to show the Pāpaku Seamount (see Fig. 1 for location and viewpoint). **a**, The 3D image with P-wave velocities superimposed. Note velocity inversion beneath the Pāpaku fault. The subducting Hikurangi basement (grey surface) peaks locally along the northern edge of the survey (Pāpaku Seamount). **b**, The same volume without seismic velocity and with interpreted thrust faults (red dashed lines) and Pāpaku fault (yellow dashed line). Light shaded areas are sediment lenses.

Superimposed on the Hikurangi basement are magnetic anomalies 25 . Note the old sediment lens has large lateral ramps in the crossline of the cutaway that form a corridor of deeply underthrust sediment in both seismic structure and velocity. \mathbf{c} , The seismic velocity along portions of the décollement obscured by vertical slices in \mathbf{a} and \mathbf{b} . Inline 175 intersects the larger low-velocity zone (LVZ-1) beneath the trailing 'corridor', while the smaller LVZ-2 lies in the wake of Seamount 2.

along Inline 175 (Fig. 4). This example exhibits the signature characteristics recognized for the Pāpaku sediment lens, specifically a 25-km-long, low-angle thrust fault with a steep lateral ramp on its northern flank that forms a domed cross section in the crossing strike profile. Furthermore, the lens sediments retain low velocities relative to the flanking and overlying strata (consistent with low velocities beneath Tuaheni thrust³⁷), and a seafloor high, the Tuaheni Ridge, lies immediately above it. The proximity of this large sediment lens to the Tuaheni Ridge (Figs. 3–5) links the origin of the ridge to past seamount collision. This, in turn, implies that the width of this sediment lens extends ~10 km south of the 3D area and into the high-slip regions of the 2014 SSE (Fig. 5). It is thus wider than that formed behind the Pāpaku Seamount, which suggests collision with a larger seamount presumed to be as tall as the thickness of this sediment lens (-3 km). A low-velocity patch also lies along the décollement beneath the sediment lens at a depth of ~7 km (Fig. 4c). Similar to the Pāpaku sediment lens, the low velocities are interpreted to result from delayed consolidation. This larger seamount lens formed at least 500,000 years ago (on the basis of the estimated time for the seamount to move from the seaward side of the sediment lens to the landward side of the 3D survey at current rates of ~53 km Myr⁻¹), and possibly much earlier (up to 1.73 million years ago³⁸). Yet despite this great age, the velocity anomaly remains, indicating that fluid drainage along and beneath the décollement can be delayed for a very long time.

A setting for slow slip

The structures revealed in the 3D seismic volume suggest that seamount collision along the northern Hikurangi margin involves a surprisingly simple sequence of processes, but ones that can have lasting impact on forearc structure, hydrogeology and slip behaviour. Collision initiates as uplift of the upper plate along the leading edge of the subducting seamount followed by overthrusting of the upper plate onto the seafloor along a long-lived trailing thrust that conforms to the cross-sectional shape of the seamount. This fault encompasses and protects a tube-shaped lens of trench sediments and, critically, appears to inhibit fluid drainage from within 36,39.

This process has broad and important implications. In contrast to seamount subduction in sediment-poor settings, the thickness of the underthrust trench sediment within the sediment lenses supports the overriding upper plate and prevents subsequent subsidence of the forearc behind the passing seamount. This configuration will limit localized normal faulting of the upper plate, reducing potential drainage pathways, in contrast to the intense normal faulting observed in the vicinity of passing seamounts elsewhere^{2,5}. Furthermore, fluid flow out of these trailing sediment lenses is likely very low due to the preference for ductile deformation within the bounding faults due to the duplication of the trench sediments by seafloor overthrusting³⁶, for example, the Pāpaku fault³⁵, and the reduced tectonic stresses in the wake of the seamounts. In combination, these preserve high fluid

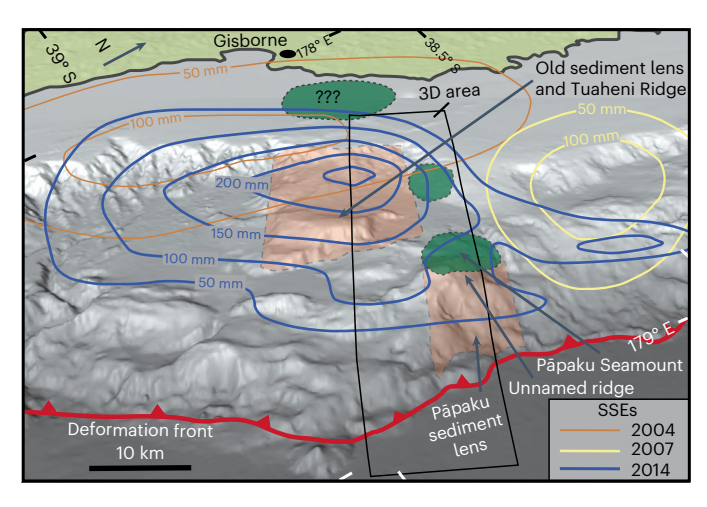


Fig. 5 | **Perspective view of the northern Hikurangi margin looking west showing seamount collisions.** Features observed and inferred from the 3D seismic reflection data, and recent SSEs. The subducted seamount (green ellipse) closest to Gisborne was not directly located but represents a subducted seamount implied by the 'old sediment lens' captured within the 3D volume. The old sediment lens lies directly beneath the Tuaheni Ridge, implicating a subducting seamount for its origin. This is the basis for inferring the lens south of the 3D survey area. The old sediment lens is collocated with the largest slip during the 2014 SSE. Light blue thick lines are canyons. Data from refs. 21,27.

volumes and overpressures³⁴ that can impact fault slip behaviour for a long time.

The occurrence and distribution of underconsolidated sediment lenses formed by seamount subduction along the Hikurangi margin provide further support for a relationship between seamounts and conditions known for generating slow slip. Source regions for SSEs and tremor have consistently been shown to coincide with high fluid pressures from geophysical observations and numerical models^{27,40–42}. Shallow SSEs, in particular, may occur where pore pressures exceed overburden by 66–95% as a result of disequilibrium compaction in low-permeability marine sediments¹⁶. These conditions are thought to be sufficient to drive faults into less-stable frictional conditions in the clay-rich sediments along the Hikurangi megathrust¹⁶. Sediments subducted ahead of seamounts have been interpreted to have those conditions²⁷. However, the underconsolidated sediments found here within sediment lenses in the wake of seamounts are also capable of sustaining elevated fluid pressures.

The difference in position of the underconsolidated sediments, lying behind rather than ahead of seamounts, is important. During SSEs, the pressure loss within the subducting crust is thought to occur in part by fluid flow into the megathrust and overriding plate^{43,44}. Overpressured zones within the sediment lenses behind the seamount may lessen pressure gradients and restrict such vertical flow, maintaining high pore pressures necessary for SSEs to occur. These anomalous features remain fixed with the upper plate, with enduring impact on the passing subducting plate. By contrast, overpressured sediments entrained within the lower plate ahead of the seamount²⁷ will continue to subduct with the seamount, eventually passing from the system. Thus, sediment lenses encased within the upper plate, especially large deeply subducted sediment lenses, can contribute to high fluid content along the décollement longer than sediments transported to depth with the seamount. Thus these upper plate features define zones that can host slow slip long after subduction of the seamount that created them.

The spatial relationships between sediment lenses and SSEs can be demonstrated with a perspective view of the northern Hikurangi margin (Fig. 5). The only SSE that has been constrained by offshore instrumentation offshore Hikurangi is the 2014 event. The highest slips

for this SSE are centred on the large sediment lens beneath Tuaheni Ridge, consistent with our model. It is more difficult to establish a link between the Pāpaku sediment lens and SSEs, which is not surprising for such a shallow sediment lens where the décollement is still in very early stages of development and may not yet host SSEs. Moreover, the 2014 SSE slip contours appear to wrap around the Pāpaku Seamount, suggesting it is an impediment to décollement slip. The large number and range of seamount sizes that occur along the Hikurangi margin (for example, refs. 45–47) imply that sediment lenses of all sizes are abundant along the margin and collectively contribute to conditions for SSEs in this setting. There is tantalizing evidence that fluid-rich sediment lenses may also exist at other subduction zones where SSEs and seamounts are collocated (for example, Nankai and Ecuador); however, existing seismic data need to be thoroughly reevaluated and, crucially, high-resolution 3D seismic data acquired.

Online content

Any methods, additional references, Nature Portfolio reporting summaries, source data, extended data, supplementary information, acknowledgements, peer review information; details of author contributions and competing interests; and statements of data and code availability are available at https://doi.org/10.1038/s41561-023-01186-3.

References

- von Huene, R., Ranero, C. R., Weinrebe, W. & Hinz, K. Quaternary convergent margin tectonics of Costa Rica, segmentation of the Cocos Plate, and central American volcanism. *Tectonics* 19, 314–334 (2000).
- 2. Dominguez, S., Lallemand, S. E., Malavieille, J. & von Huene, R. Upper plate deformation associated with seamount subduction. *Tectonophysics* **293**, 207–224 (1998).
- Dominguez, S., Malavieille, J. & Lallemand, S. E. Deformation of accretionary wedges in response to seamount subduction: insights from sandbox experiments. *Tectonics* 19, 182–196 (2000).
- Park, J.-O., Tsuru, T., Kaneda, Y. & Kono, Y. A subduction seamount beneath the Nankai accretionary prism off Shikoku, southwestern Japan. Geophys. Res. Lett. 26, 931–934 (1999).
- Ruh, J. B., Sallarès, V., Ranero, C. R. & Gerya, T. Crustal deformation dynamics and stress evolution during seamount subduction: high-resolution 3-D numerical modeling. J. Geophys. Res. Solid Earth 121. 6880–6902 (2016).
- Park, J. O., Tsuru, T., Kodaira, S., Cummins, P. R. & Kaneda, Y. Splay fault branching along the Nankai subduction zone. Science 297, 1157–1160 (2002).
- Moore, G.F. et al. Structural and seismic stratigraphic framework of the NanTroSEIZE Stage 1 transect. In Proc. Integrated Ocean Drilling Program Vol. 314/315/316 (eds Kinoshita, M. et al.) 1–46 (International Ocean Discovery Program, 2009).
- Morgan, J. K. & Bangs, N. L. Recognizing seamount-forearc collisions at accretionary margins: insights from discrete numerical simulations. *Geology* 45, 635–638 (2017).
- Sun, T., Saffer, D. & Ellis, S. Mechanical and hydrological effects of seamount subduction on megathrust stress and slip. *Nat. Geosci.* 13, 249–255 (2020).
- Wallace, L. M., Beavan, J., McCaffrey, R. & Darby, D. Subduction zone coupling and tectonic block rotations in the North Island, New Zealand. J. Geophys. Res. 109, B1240 (2004).
- Jiang, Y. S. et al. Slow slip events in Costa Rica detected by continuous GPS observations, 2002–2011. Geochem. Geophys. Geosyst 13, Q04006 (2012).
- 12. Nishimura, T. Short-term slow slip events along the Ryukyu Trench, southwestern Japan, observed by continuous GNSS. *Prog. Earth Planet. Sci.* **1**, 22 (2014).
- Kato, A. et al. Propagation of slow slip leading up to the 2011 M_w
 9.0 Tohoku-Oki earthquake. Science 335, 705–708 (2012).

- Scholz, C. H. & Small, C. The effect of seamount subduction on seismic coupling. *Geology* 25, 487–490 (1997).
- Wang, K. & Bilek, S. L. Do subducting seamounts generate or stop large earthquakes? Geology 39, 819–822 (2011).
- Saffer, D. M. & Wallace, L. M. The frictional, hydrologic, metamorphic and thermal habitat of shallow slow earthquakes. *Nat. Geosci.* 8, 594–600 (2015).
- Vallee, M. et al. Intense interface seismicity triggered by a shallow slow slip event in the Central Ecuador subduction zone. J. Geophys. Res. Solid Earth 118, 2965–2981 (2013).
- Sage, F., Collot, J.-Y. & Ranero, C. R. Interplate patchiness and subduction-erosion mechanisms: evidence from depth-migrated seismic images at the central Ecuador convergent margin. Geology 34, 997–1000 (2006).
- Kimura, G. et al. Rejuvenated extension of the Philippine Sea plate and its effect on subduction dynamics in the Nankai Trough. Isl. Arc 30, e12402 (2021).
- Schwartz, S. Y. & Rokosky, J. M. Slow slip events and seismic tremor at circum-Pacific subduction zones. Rev. Geophys. 45, RG3004 (2007).
- Wallace, L. M. et al. Slow slip near the trench at the Hikurangi subduction zone, New Zealand. Science 352, 701-704 (2016).
- Barnes, P. M. et al. 2020 Slow slip source characterized by lithological and geometric heterogeneity. Sci. Adv. 6, eaay3314 (2020).
- Crundwell, M. P. & Woodhouse, A. Biostratigraphically constrained chronologies for Quaternary sequences from the Hikurangi margin of north-eastern Zealandia. N. Z. J. Geol. Geophys. https://doi.org/10.1080/00288306.2022.2101481 (2022).
- Bell, R., Holden, C., Power, W., Wang, X. & Downes, G. Hikurangi margin tsunami earthquake generated by slow seismic rupture over a subducted seamount. *Earth Planet. Sci. Lett.* 397, 1–9 (2014).
- Barker, D. H. N. et al. Geophysical constraints on the relationship between seamount subduction, slow slip, and tremor at the north Hikurangi subduction zone, New Zealand. Geophys. Res. Lett. 45, 12804–12813 (2018).
- Chesley, C., Naif, S., Key, K. & Bassett, D. Fluid-rich subducting topography generates anomalous forearc porosity. *Nature* 595, 255–260 (2021).
- Bell, R. et al. Seismic reflection character of the Hikurangi subduction interface, New Zealand, in the region of repeated Gisborne slow slip events. *Geophys. J. Int.* 180, 34–48 (2010).
- 28. Bangs, N. L., Gulick, S. P. S. & Shipley, T. H. Seamount subduction erosion in the Nankai Trough and its potential impact on the seismogenic zone. *Geology* **34**, 701–704 (2006).
- Saffer, D.M. et al. Site U1518. In Hikurangi Subduction Margin Coring, Logging, and Observatories. Proceedings of the International Ocean Discovery Program, 372B/375 (eds Wallace, L.M. et al.) (2019); https://doi.org/10.14379/iodp. proc.372B375.103.2019
- 30. Arai, R. et al. Team three-dimensional P wave velocity structure of the northern Hikurangi margin from the NZ3D experiment: evidence for fault-bound anisotropy. *J. Geophys. Res. Solid Earth* **125**, e2020JB020433 (2020).
- Cook, A. E. et al. Physical properties and gas hydrate at a near-seafloor thrust fault, Hikurangi margin, New Zealand. Geophys. Res. Lett. 47, e2020GL088474 (2020).
- Solomon, E. A. et al. Geochemical constraints on fluid-rock reactions, fluid sources, and flow pathways along the IODP Expedition 375 transect; northern Hikurangi margin. 2018 Am. Geophys. Fall Meeting abstr. T54C-07 (2018).

- Saffer, D. M. et al. Expedition 372B/375 summary. In Hikurangi Subduction Margin Coring, Logging, and Observatories. Proceedings of the International Ocean Discovery Program, 372B/375 (eds Wallace, L.M. et al.) (2019); https://doi.org/ 10.14379/iodp.proc.372B375.101.2019
- French, M. E. & Morgan, J. K. Pore fluid pressures and strength contrasts maintain frontal fault activity, northern Hikurangi margin, New Zealand. Geophys. Res. Lett. 47, e2020GL089209 (2020).
- Fagereng, Å. et al. Mixed deformation styles observed on a shallow subduction thrust, Hikurangi margin, New Zealand. Geology 47, 872–876 (2019).
- Morgan, J. K. et al. Seafloor overthrusting causes ductile fault deformation and fault sealing along the northern Hikurangi margin. Earth Planet. Sci. Lett. 593, 117651 (2022).
- 37. Gase, A. C. et al. Crustal structure of the northern Hikurangi margin, New Zealand: variable accretion and overthrusting plate strength influenced by rough subduction. *J. Geophys. Res. Solid Earth* **126**, e2020JB021176 (2021).
- 38. Tilley, H., Moore, G.F., Bangs, N., Han, S., & Barnes, P. Deformation of an intraslope basin above the site of slow earthquakes at the Hikurangi subduction margin. 2018 Am. Geophys. Fall Meeting abstr. T21A-06 (2018).
- 39. Aretusini, S., Meneghini, F., Spagnuolo, E., Harbord, C. W. & Di Toro, G. Fluid pressurisation and earthquake propagation in the Hikurangi subduction zone. *Nat. Commun.* **12**, 2481 (2021).
- 40. Bassett, D., Sutherland, R. & Henrys, S. Slow wavespeeds and fluid overpressure in a region of shallow geodetic locking and slow slip, Hikurangi subduction margin, New Zealand. *Earth Planet. Sci. Lett.* **389**, 1–13 (2014).
- 41. Araki, E. et al. Recurring and triggered slow-slip events near the trench at the Nankai Trough subduction megathrust. *Science* **356**, 1157–1160 (2017).
- 42. Ellis, S. et al. Fluid budgets along the northern Hikurangi subduction margin, New Zealand: the effect of a subducting seamount on fluid pressure. *Geophys. J. Int.* **202**, 277–297 (2015).
- 43. Warren-Smith, E. et al. Episodic stress and fluid pressure cycling in subducting oceanic crust during slow slip. *Nat. Geosci.* **12**, 475–481 (2019).
- 44. Nakajima, J. & Uchida, N. Repeated drainage from megathrusts during episodic slow slip. *Nat. Geosci.* **11**, 351–356 (2018).
- 45. Collot, J.-Y., Lewis, K., Lamache, G. & Lallemand, S. The giant Ruatoria debris avalanche on the northern Hikurangi margin, New Zealand: result of oblique seamount subduction. *J. Geophys. Res.* **106**, 19271–19279 (2001).
- Pedley, K. L., Barnes, P. M., Pettinga, J. R. & Lewis, K. B. Seafloor structural geomorphic evolution of the accretionary frontal wedge in response to seamount subduction, Poverty Indentation, New Zealand. *Mar. Geol.* 270, 119–138 (2010).
- 47. Chow, B., Kaneko, Y. & Townend, J. Evidence for deeply subducted lower-plate seamounts at the Hikurangi subduction margin: implications for seismic and aseismic behavior. *J. Geophys. Res. Solid Earth* **127**, e2021JB022866 (2022).

Publisher's note Springer Nature remains neutral with regard to jurisdictional claims in published maps and institutional affiliations.

Springer Nature or its licensor (e.g. a society or other partner) holds exclusive rights to this article under a publishing agreement with the author(s) or other rightsholder(s); author self-archiving of the accepted manuscript version of this article is solely governed by the terms of such publishing agreement and applicable law.

@ The Author(s), under exclusive licence to Springer Nature Limited 2023

¹Institute for Geophysics, Jackson School of Geosciences, University of Texas at Austin, Austin, TX, USA. ²Department of Earth, Environmental and Planetary Sciences, Rice University, Houston, TX, USA. ³Department of Earth Science and Engineering, Imperial College, London, UK. ⁴Japan Agency for Marine–Earth Science and Technology, Yokohama, Japan. ⁵School of Earth and Space Sciences, University of Science and Technology of China, Hefei, China. ⁶Department of Earth Sciences, University of Hawai'i at Manoa, Honolulu, HI, USA. ⁷Marinespace, Southampton, UK. ⁸GNS Science, Lower Hutt, New Zealand. ⁹Department of Earth and Planetary Sciences, University of California, Santa Cruz, CA, USA. ¹⁰Zanskar Geothermal & Minerals, Inc, Salt Lake City, UT, USA. ¹¹Department of Earth and Space Science, University of Washington, Seattle, WA, USA. ¹²School of Geography, Earth and Environmental Science, University of Birmingham, Birmingham, UK. ⊠e-mail: nathan@ig.utexas.edu

Methods

Seismic-data acquisition

Data acquisition. This project used the RV Tangaroa (cruises TAN1712 and TAN1803) and the RV Langseth (MGL1801) to acquire 3D seismic reflection and refraction data along the Hikurangi margin offshore Gisborne, New Zealand, between 6 January and 8 February 2018. From the RV *Tangaroa*, we deployed 97 OBSs provided by the Japan Agency for Marine–Earth Science and Technology (JAMSTEC) with nominal 2 km randomized spacing within the 15 × 60 km survey area. The OBSs recorded three components and hydrophone pressure signals during the seismic operations. The surface streamer data were acquired on the RV Langseth using four 6 km, 468-channel streamers towed with 150 m spacing at 8 m depth below the sea surface. We used two tuned source arrays of 18 airguns with 3,300 inch³ (54 l) each towed with 75 m separation at 7 m depth and shot in an alternating 'flip-flop' pattern at 25 m intervals between shots. We made 62 passes through the survey area for a total sail line length of 5,489 km and fired 143,078 shots recorded simultaneously on streamers and OBS.

Processing. The processing consisted of three main efforts: (1) pre-processing to remove unwanted components and prepare data for depth imaging migration, (2) tilted transverse isotropy (TTI) depth velocity model building and (3) depth imaging. This processing was conducted by a commercial contractor, CGG Services PTE LTD.

Pre-processing for the results presented here was as follows: data resampling to 4 ms, correcting navigation, trace editing to remove bad traces, low-frequency noise suppression, recording delay correction, swell noise attenuation and despiking, tidal statics, water-column statics correction, shot and channel scaling, receiver motion correction to correct for moving streamer position during recording, linear noise attenuation across shot gathers, joint 3D source and receiver deghosting and designature, gun/streamer static correction, model-based water demultiple with water bottom modelling, iterative 3D surface-related multiple elimination, simultaneous subtraction of model-based water demultiple with water bottom modelling and surface-related multiple elimination, velocity analysis at 2 × 2 km spacing and Radon demultiple on 2D common midpoint (CMP) gathers, attenuation analysis and compensation (phase only), 3D binning and data regularization, diffraction multiple attenuation, acquisition footprint removal and offset domain denoise.

A starting velocity model was generated from stacking velocity analysis, and this model was updated using reflection tomography and full-waveform inversion. Throughout the process, flattening of reflections in common image gathers (CIG), as well as improvements in the prestack depth migration, were used for quality control. Initial inversions (Supplementary Fig. 12 and Extended Data Fig. 7) were isotropic and applied to refractions recorded on the streamer and OBS, whereas later inversions also included reflections, TTI anisotropy and an anomalous low-Q (low quality factor, high attenuation) zone below the bottom-simulating reflection. In the final model shown in Figs. 3 and 4, TTI full-waveform inversion was run up to 12 Hz, and a TTI tomographic inversion was used to further refine the deeper velocity structure (>3.5 km below the seabed). Constraints on the low-velocity zones shown in Figs. 3 and 4 were established by flattening CIGs (Supplementary Fig. 11 and Extended Data Fig. 8) and tracking the improvements to migrated images. We note that there are differences between the deeper (>6 km depth) velocity model presented here and that shown in ref. 30. These differences arise from considerations of anisotropy, the scanning tomography used here, and flattening of reflections in CIGs done in this study versus the isotropic refraction tomography of ref. 30. Fits to the data are shown in Supplementary Fig. 9 (Extended Data Fig. 9) and in the data processing report⁴⁸.

We conducted the depth imaging using a 3D Kirchhoff migration algorithm and the TTI velocity model described with a 5 km half aperture and 12.5 crossline and 18.75 m inline spacing. Results were converted to time domain for a velocity analysis on a 50 m \times 50 m grid at 20 ms depth interval and time-domain enhancements. CIGs were then flattened and Radon demultiple applied. This was followed by residual denoise, diffraction noise attenuation, spectral offset balancing, angle mute, frequency-dependent amplitude correction for spatial amplitude balancing, bandwidth enhancement, footprint removal, time varying filter and scaling, and time-to-depth conversion. Improvements to the images from initial to final results are shown in Supplementary Fig. 13 (Extended Data Fig. 10).

Data availability

Raw seismic reflection data are available at https://doi.org/10.1594/IEDA/324554 (ref. 49). The processed 3D PSDM data used in interpretation are available at https://doi.org/10.26022/IEDA/331022 (ref. 50). The seismic velocity model produced from 3D full-waveform inversion and used in the interpretation are available at https://doi.org/10.26022/IEDA/331023 (ref. 51). Ocean-bottom seismometer data are available via https://www.jamstec.go.jp/rimg/e/. Bathymetry data are available via https://niwa.co.nz/oceans/tools-and-resources. All data from MGL1801 (Cruise DOI: 10.7284/907876) are available at https://www.marine-geo.org/tools/search/entry.php?id=MGL1801.

References

- NZ3D data processing team. NZ3D seismic data processing report. (Marine Geoscience Data Systems, 2022); https://www.marine-geo.org/tools/search/Document_Accept.php?client=DataLink&doc uid=4871&entry id=MGL1801
- Bangs, N. et al. Multi-Channel Seismic Shot Data from the Hikurangi Subduction Margin Collected During R/V Marcus G. Langseth Expedition MGL1801 (Interdisciplinary Earth Data Alliance, 2018); https://doi.org/10.1594/IEDA/ 324554
- Bangs, N. et al. NZ3D Seismic Reflection Data Volume Prestack Depth Migration (PSDM) (Interdisciplinary Earth Data Alliance, 2022); https://doi.org/10.26022/IEDA/331022
- Bangs, N. et al. NZ3D Velocity Data Volume 3D TTI Full Waveform Inversion (3DTTIFWI) (Interdisciplinary Earth Data Alliance, 2022); https://doi.org/10.26022/IEDA/331023
- Thomsen, L. Weak elastic anisotropy. *Geophysics* 51, 1954–1966 (1986).

Acknowledgements

We thank the captains, crew and onboard science parties of the RV *Tangaroa* and the RV *Marcus G. Langseth* for their contribution to the data acquisition. We thank Paradigm Geophysical for providing software. We thank NIWA for providing bathymetry data. The academic NZ3D project was financially supported by US NSF (award #s 1559298 (N.L.B., S.H. and A.C.G.), 1901645 (N.L.B. and S.H.), 1559008 (G.F.M. and H.L.T.), 2023186 (G.F.M. and H.L.T.), 1558574 (H.J.T.) and 1558440 (J.H.E.)), NERC NE/M021203/1 (R.E.B., R.D. and L.F.), JAMSTEC (R.A. and S.K.), NZ MBIE and GNS Science (D.H.N.B., S.A.H., D.B., R.K., V.S. and B.F.).

Author contributions

N.L.B., R.E.B., S.K., R.A. and S.A.H., designed the experiment. N.L.B., S.H. H.L.T., D.H.N.B., J.H.E, H.J.T, T.J.R. D.B. R.K., V.S. and B.F. helped with data acquisition at sea on the RV *Lanseth* or RV *Tangaroa*. N.L.B. and S.H. directed CGG in data processing. N.L.B., J.K.M., S.H., A.C.G. and X.W. conducted the data interpretation. R.E.B., R.D. and L.F. conducted initial full-waveform inversions. All authors contributed to the writing of this manuscript.

Competing interests

The authors declare no competing interests.

Additional information

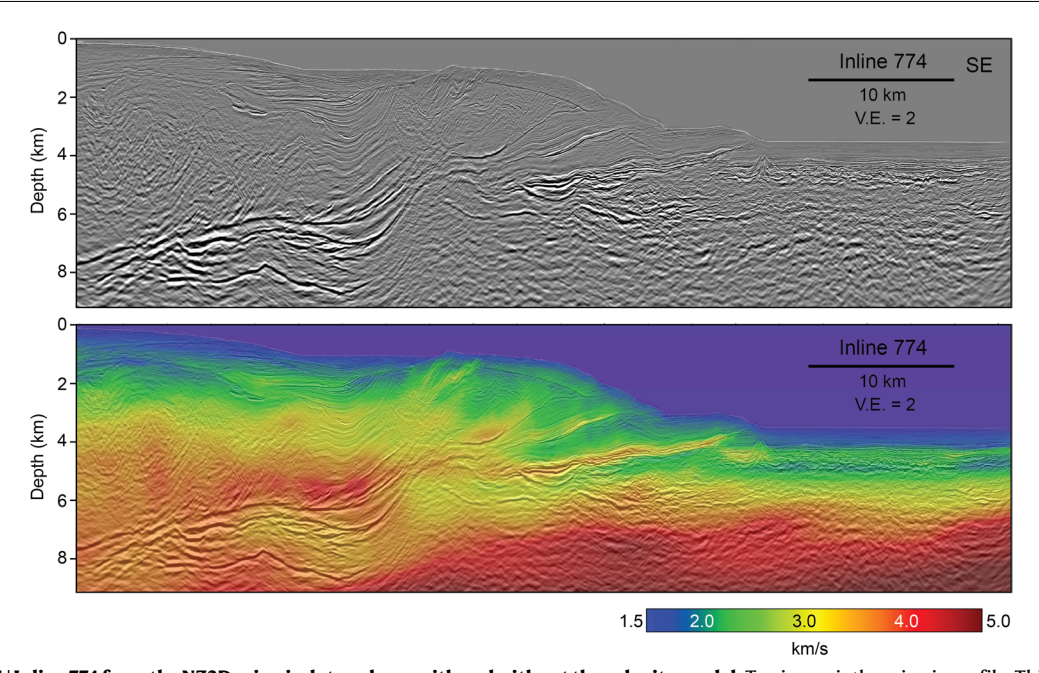
Extended data is available for this paper at https://doi.org/10.1038/s41561-023-01186-3.

Supplementary information The online version contains supplementary material available at https://doi.org/10.1038/s41561-023-01186-3.

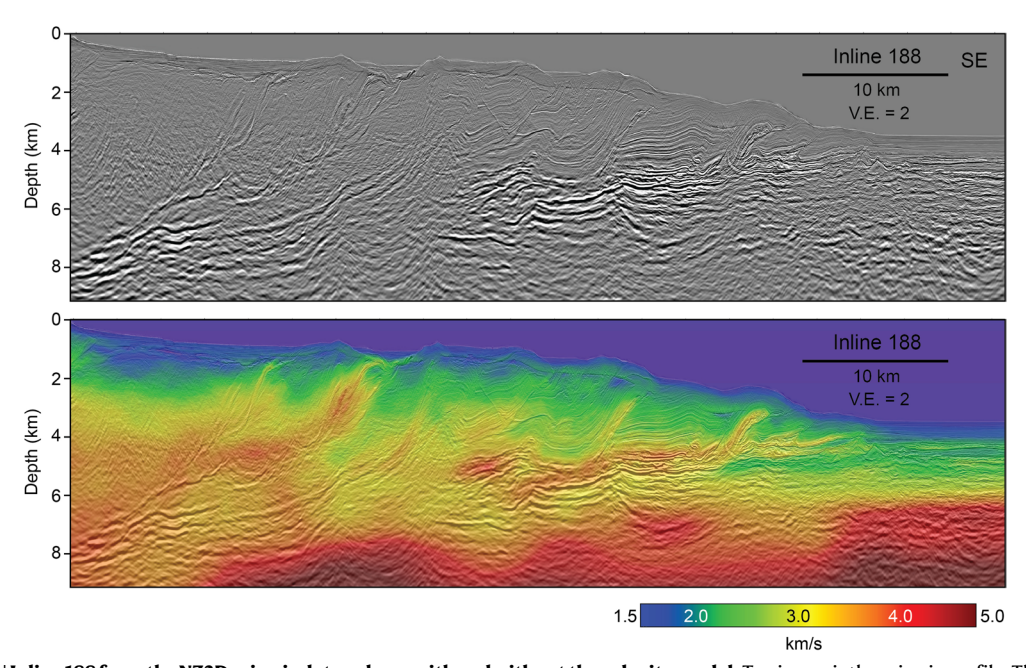
Correspondence and requests for materials should be addressed to Nathan L. Bangs.

Peer review information *Nature Geoscience* thanks Jacob Geersen, Jean-yves Collot and the other, anonymous, reviewer(s) for their contribution to the peer review of this work. Primary Handling Editor: Louise Hawkins, in collaboration with the *Nature Geoscience* team.

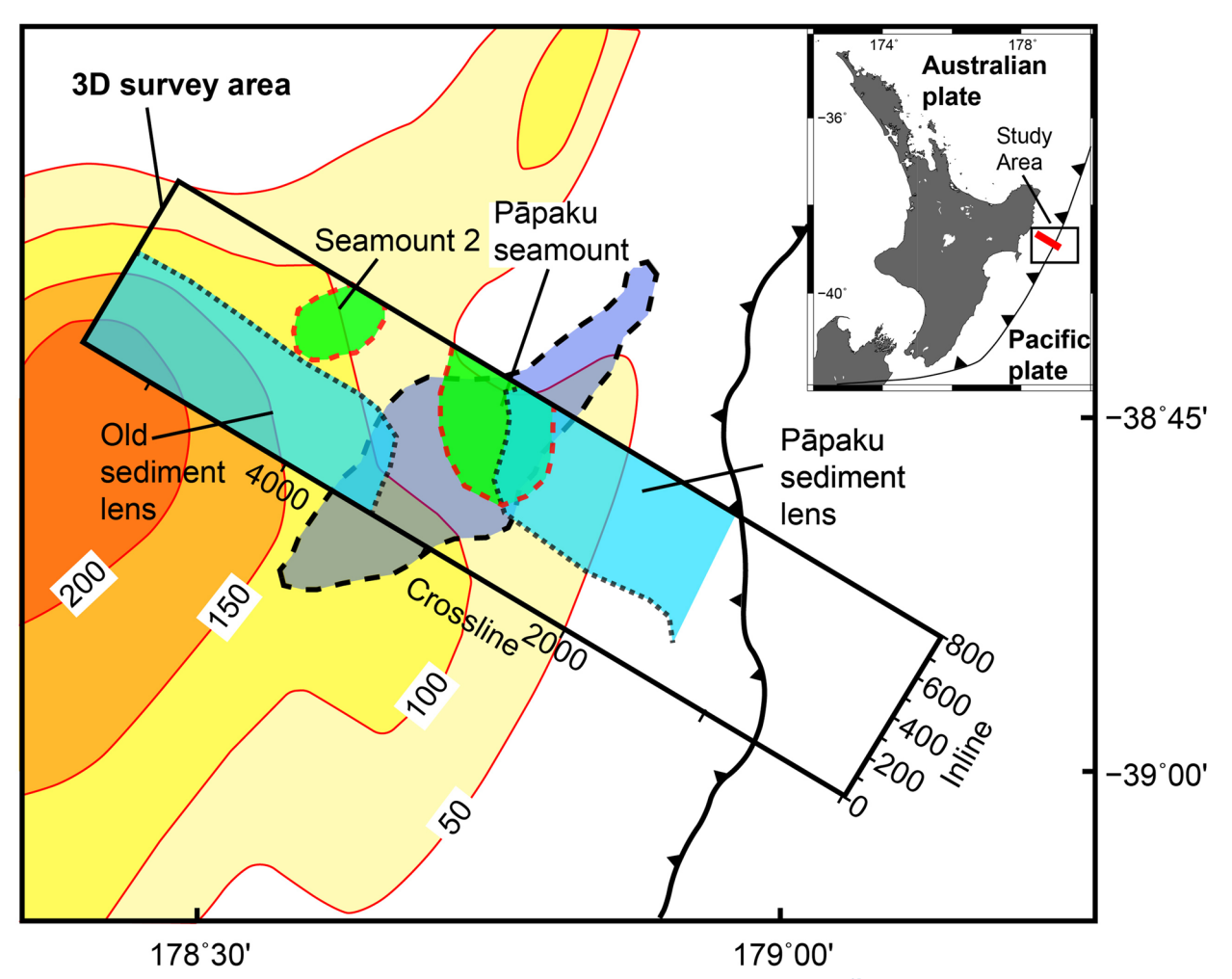
Reprints and permissions information is available at www.nature.com/reprints.



 $\textbf{Extended Data Fig. 1} | \textbf{Inline 774 from the NZ3D seismic data volume with and without the velocity model.} Top image is the seismic profile. This is the same line as shown in Fig. 2, but without interpretation. Bottom section has an overlay of the velocity model. See Fig. 1 for location.}$

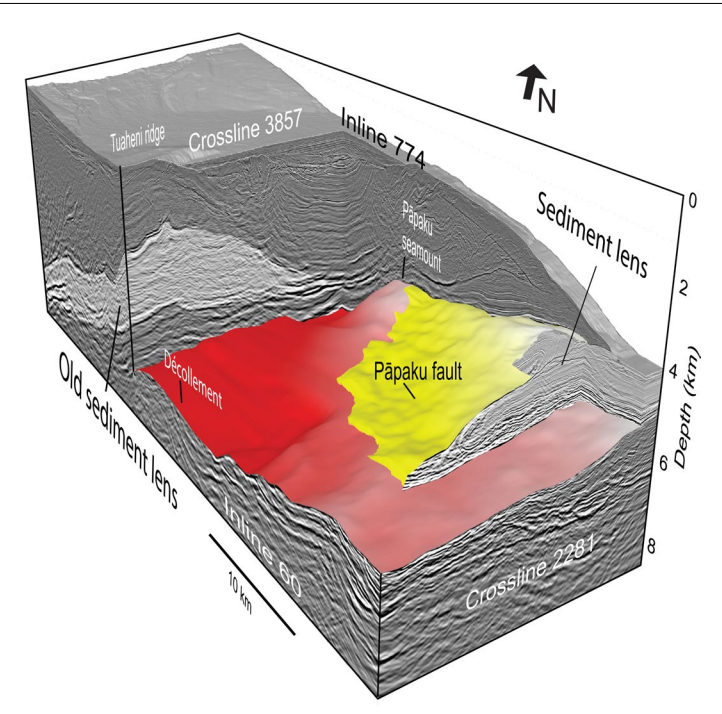


 $\textbf{Extended Data Fig. 2} | \textbf{Inline 188 from the NZ3D seismic data volume with and without the velocity model.} Top image is the seismic profile. This is the same line as shown in Fig. 2, but without interpretation. Bottom section has an overlay of the velocity model. See Fig. 1 for location.}$



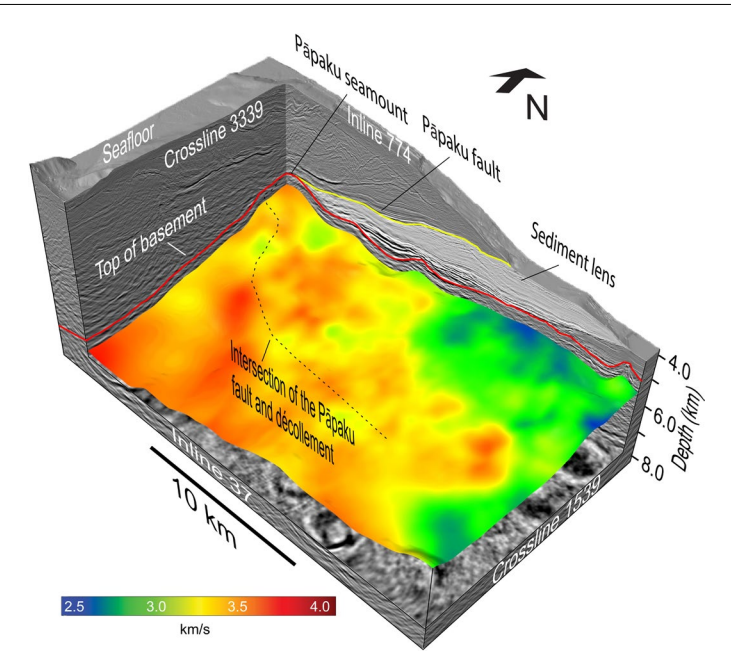
Extended Data Fig. 3 | Map showing locations of features discussed in the **text.** Map directly overlaps with Fig. 1 and shows the seamounts and sediment lenses in NZ3D survey area (black rectangle), and slip during the 2014 slow slip event 21 . Barbed black line marks the deformation front. The NZ3D survey is $15 \times 65 \, \mathrm{km}^2$. Red dashed lines (with green shading) are seamount locations imaged within the 3D volume. Dark blue shading shows the outline of an inferred

seamount from Barker et al. 25) based on a two-dimensional seismic profile and magnetic anomalies. Cyan shading shows the position of a sediment lens in the wake of the Pāpaku seamount and beneath the Pāpaku fault, and second sediment lens believed to have formed from an older, subducted seamount. Slip contours are in mm.



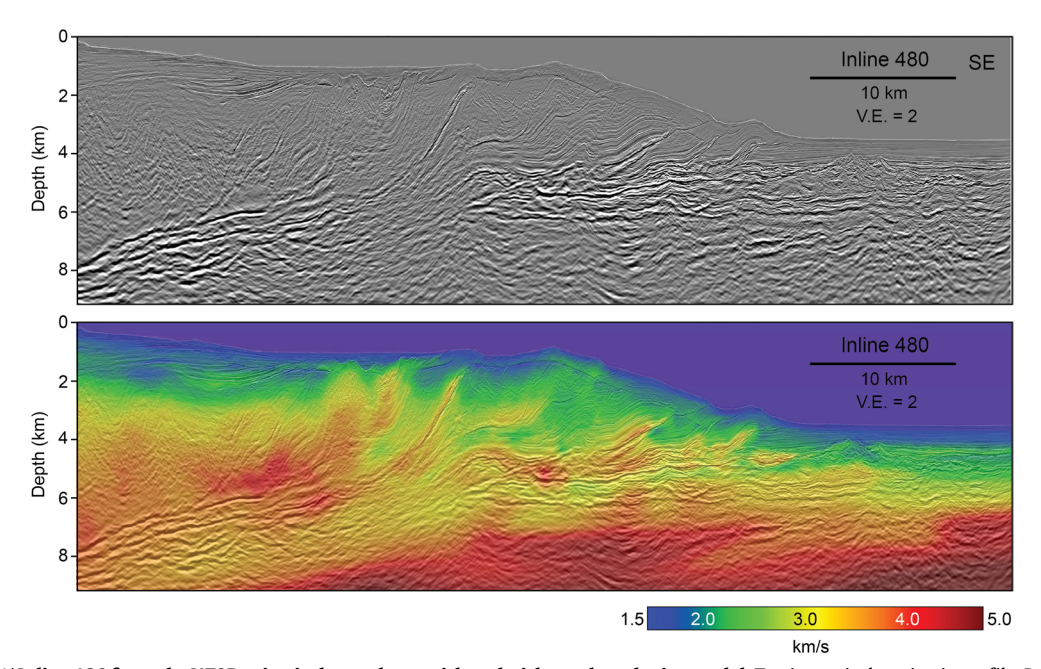
Extended Data Fig. 4 | **Three-dimensional perspective view showing the sediment lens geometry.** This view looks north and shows the seismic data volume with the sediment lens (light shading) updip from the Pāpaku seamount. The Pāpaku sediment lens formed in the wake of the subducting Pāpaku seamount. The yellow surface is the Pāpaku fault, which forms a lateral ramp that intersects the décollement in an arcuate pattern. It extends farthest

downdip above the Pāpaku seamount peak. The sediment lens beneath the Pāpaku fault fills in the space updip from the Pāpaku seamount. The peak of the Pāpaku seamount lies directly updip from the thickest section of the sediment lens, which thins to the SW updip of the flank of the Pāpaku seamount. A second sediment lens lies beneath Tuaheni ridge and is believed to have formed from an older subducted seamount.

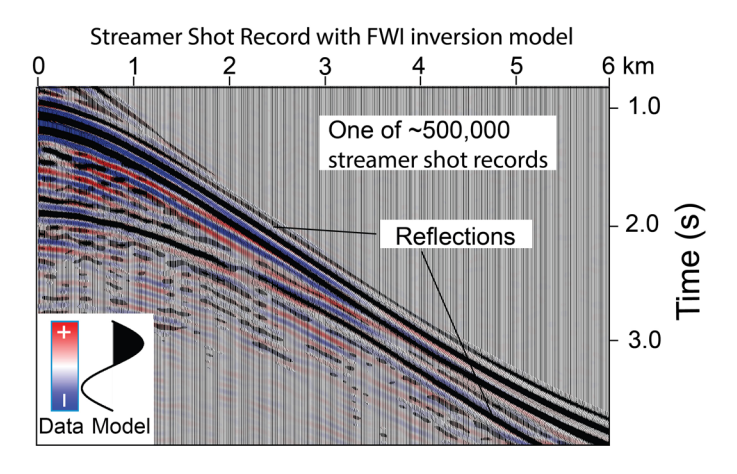


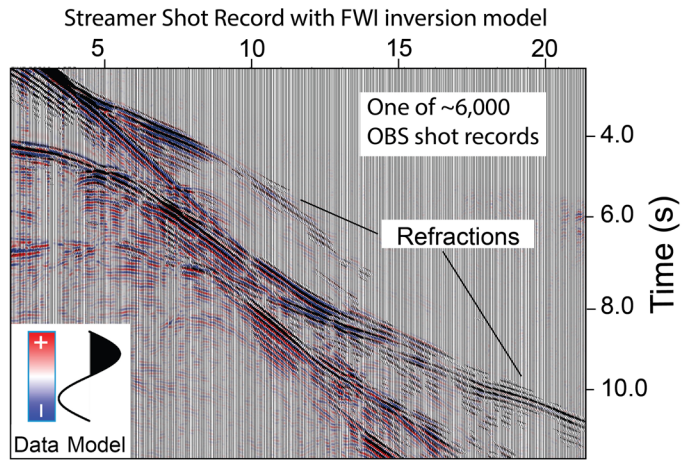
Extended Data Fig. 5 | Perspective view showing the sediment lens beneath the Pāpaku fault and underlying basement seismic velocities. Light shading shows the geometry of the sediment lens beneath the Pāpaku fault. The colored surface lies $500 \, \text{m}$ below the top of the subducting basement (red line) and shows the average velocity within the uppermost $500 \, \text{m}$ of subducting basement.

Basement velocities are consistently lower beneath the sediment lens associated with the Pāpaku seamount than regions outside of the influence of the sediment lens to the southwest. This correlation suggests that the sediment lens inhibits drainage from beneath it.



Extended Data Fig. 6 | Inline 480 from the NZ3D seismic data volume with and without the velocity model. Top image is the seismic profile. Bottom section has an overlay of the velocity model. Inline 480 is located mid-way between Inlines 188 and 774, which are located in Fig. 1. This line lies - 350 m south of the IODP Expedition 372/375 drilling transect.



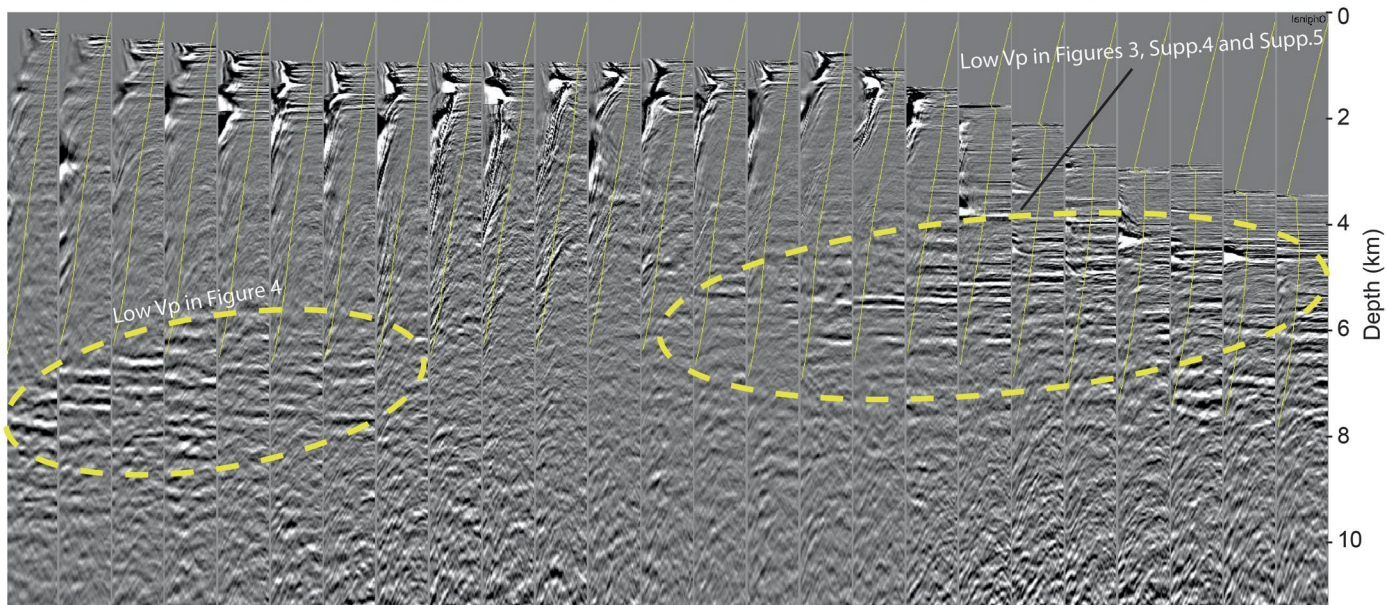


Extended Data Fig. 7 | **Full-waveform inversion models of streamer and OBS records.** Surface streamer shot record (top) and a portion of an OBS shot record (bottom) with an FWI model from inversion up to 7 Hz superimposed on top. The positive lobe of the signal is shaded in black and the negative left unshaded to

show where fit is good (blue showing) and poor (red showing). Models of both the reflections in the shot records and refractions in the OBS records fit the data well, and were further improved in subsequent inversions.

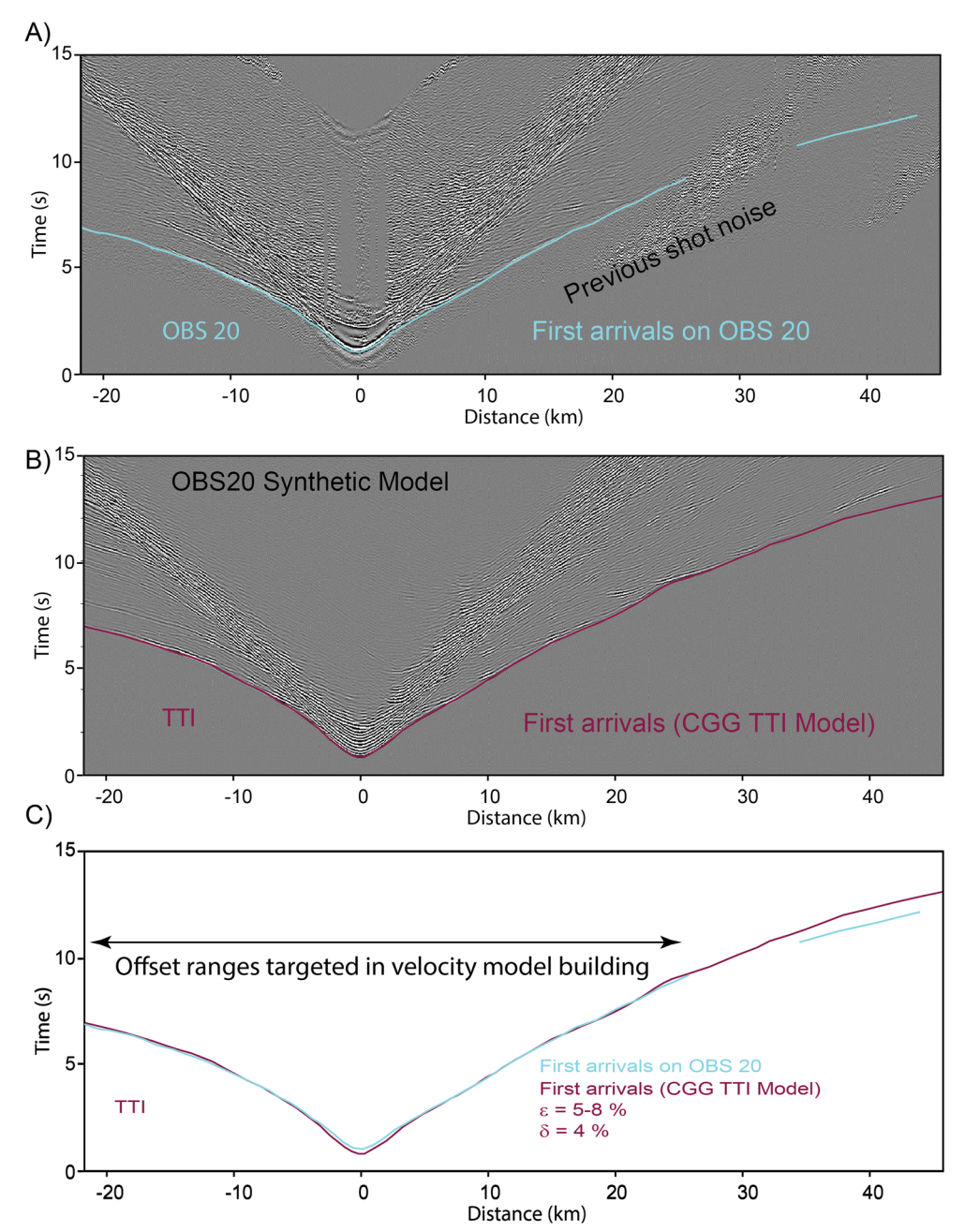
Flattened Gathers Inline 500

Xline 5157 4997 4837 4677 4517 4357 4197 4037 3877 3717 3557 3397 3237 3077 2917 2757 2597 2437 2277 2177 1957 1797 1637 1477 1317



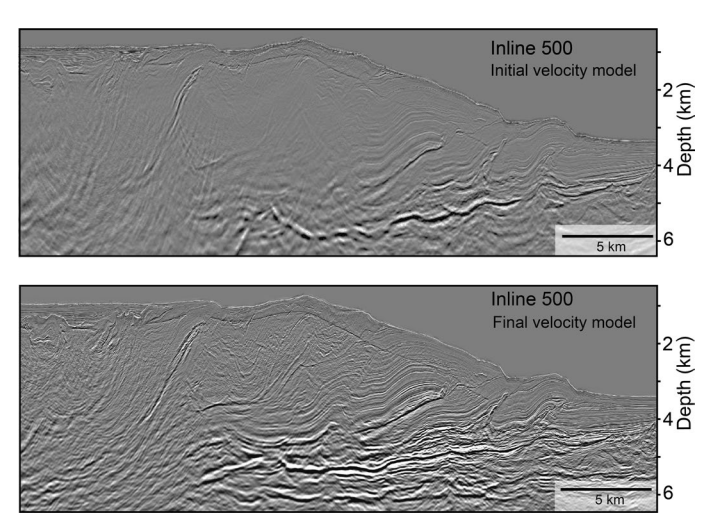
Extended Data Fig. 8 | Common image gathers (CIG) across Inline 500 showing the flattening of deep events following depth migration using the FWI/tomographic inversion model. Gathers are flattened across the

full range of offsets within depths equivalent to regions interpreted in Figs. 3, 4, Supplementary Figs. 4 $\&\,5$. These flattened gathers help validate the velocity model.



Extended Data Fig. 9 | OBS20 geophone record showing first arrivals and the corresponding model result. Shown is one record from one of 97 OBS used in the FWI and tomographic inversion. a) OBS20 record with first arrivals picked (blue line) to compare with synthetic model. b) Synthetic model produced from FWI and tomographic inversion of OBS 20. First arrival picked (red line) to compare with data. c) Comparison of first arrivals from OBS 20 and synthetic

seismogram derived from FWI and tomographic inversion by CGG Services (Singapore) showing excellent agreement at all offset ranges out to -25 km. FWI was limited to 25 km offsets due to previous shot noise and weak signals at higher offsets. ϵ and δ are Thomsen anisotropy parameters 52 . See Arai et al. 30 for location.



Extended Data Fig. 10 | Comparison of the initial and the final images for Inline 500. The initial (top) and the final (bottom) images for Inline 500 produced with initial and final velocity models to show improved continuity

of major reflections, reduced interference from reflections crosscutting primary reflections, higher reflection amplitudes, and more geologically realistic structures.